ELSEVIER

Journal of Fluids and Structures 25 (2009) 1049–1064

JOURNAL OF FLUIDS AND STRUCTURES

www.elsevier.com/locate/jfs

Deformation of a fluid-filled compliant cylinder in a uniform flow

M. Yokoyama[a,*], O. Mochizuki[b]

[a]*Department of Intelligent Material and Mechatronics Systems, Toyo University, Kujirai 2100, Kawagoe, Saitama 350-8585, Japan*
[b]*Department of System Robotics, Faculty of Engineering, Toyo University, Kujirai 2100, Kawagoe, Saitama 350-8585, Japan*

Received 20 May 2008; accepted 14 May 2009
Available online 5 July 2009

Abstract

We investigated surface compliance effects of a fluid-filled object in flow on its shape and internal flow through numerical simulation. A two-dimensional compliant cylinder containing fluid in a flow is a simple model of a cell, e.g. an erythrocyte, leukocyte or platelet. The thin membrane of the cylinder consisted of a network of mass-spring-damper (MSD) systems, representing its mechanical characteristics. We assumed that the stiffness and damping coefficients were those of latex gum. The two-dimensional flow inside and outside the membrane was obtained by solving the two-dimensional Navier–Stokes equations by using the finite element scheme at $Re = 400$, based on the external flow velocity and diameter of an initial circular cylinder. The deformation of the membrane was calculated by solving the equation of motion for an MSD system by using the fourth-order Runge-Kutta method. The compliant cylinder deformed more if its stiffness was smaller than that of latex gum. The initial circular section of the cylinder became oval, with a flat front and a convex rear. The aspect ratio of the lateral to streamwise axis length of the oval became larger than unity, and increased with decreasing stiffness. The drag coefficient of the oval cylinder became larger than that of the circular cylinder, and increased with decreasing stiffness. The partial vibration at the rear, caused by shedding vortices, induced oscillating internal flows between two antinodes of the vibrating membrane. Since the object with smaller stiffness had higher ductility, velocity fluctuations of the external flow influenced the internal flow of the compliant object through deformation of the membrane.

Keywords: Deformation; Fluid dynamics; Numerical simulation; Coupling problem; Compliant cylinder; Membrane

1. Introduction

The objective of this study is to investigate deformation of a fluid-filled compliant object in a flow. In this study, a two-dimensional compliant cylinder, filled with an incompressible Newtonian liquid, is placed in a two-dimensional uniform flow, of the same liquid as is inside the compliant cylinder. This is a simple model of a cell, e.g. erythrocyte, leukocyte or platelet, in a flow. Our goal is to understand how a cell is deformed by stresses due to the external flow, and how the deformation affects protoplasmic flow in a cell. Numerical simulation is a useful method for surveying parametric effects of mechanical properties of the membrane with both external and internal flows. Large deformations

*Corresponding author. Tel./fax: +81 48 461 1390.
E-mail address: master@cello-maker.com (M. Yokoyama).

0889-9746/$ - see front matter
doi:10.1016/j.jfluidstructs.2009.05.006

Nomenclature

Symbols related to the structure of the object

AR	aspect ratio defined by L_y/L_x
c	damping coefficient
k	spring constant
L_x	maximum length in the X-axis after deformation
L_y	maximum length in the Y-axis after deformation
$m_{\mathrm{in},i}$, $m_{\mathrm{out},i}$	internal mass and external mass ($i = 0,\ldots,N_m-1$, $N_m = 48$)
M	total mass of the compliant cylinder (sum of $m_{\mathrm{in},i}$, $m_{\mathrm{out},i}$ and the internal fluid ($= \rho_{\mathrm{in}}\pi R^2$))
R	radius of the initial circular cylinder
T_K	shedding period of vortices
T_N	period of the natural vibration of the compliant cylinder
T_C	convergence time when the change in AR becomes smaller than $h = 0.001L_y$
T_F	required time to reach the final shape
w	width of calculation domain

Symbols related to the flow

C_d	drag coefficient ($=$ Drag$/\rho RU^2$)
dt^*	time step $= 0.01$ which is determined as to satisfy the Courant number
p_{in}, p_{out}	pressures acting on the inside and outside surfaces of the membrane
Re	Reynolds number ($= 2UR/\nu$)
St	Strouhal number ($=$ N2R/U, N: number of shedding vortices per unit time)
t^*	nondimensional time ($= Ut/2R$, where t is a time measured in seconds)
U	free-stream velocity
u, v	components of flow velocity in the x and y directions
ν_{in}, ν_{out}	kinematic viscosities of the internal and external fluids (in the present study, $\nu_{\mathrm{in}} = \nu_{\mathrm{out}}$),
ρ_{in}, ρ_{out}	densities of the internal and external fluids (in the present study, $\rho_{\mathrm{in}} = \rho_{\mathrm{out}}$)
τ_{in}, τ_{out}	shearing stresses acting on the inside and outside surfaces of the membrane
φ	stream function
φ_B	boundary stream function
ω	vorticity

of elastic cylindrical capsules in shear flows were solved by a series-expansion technique by Rao et al. (1994). Dependence of deformation and apparent viscosity, on strain rate was discussed. Deformations become large if strain rate increases, and small if internal viscosity increases. Since the ductility of red blood cells (RBC) is related to health conditions and diseases, it is important to understand the interaction between internal flow, external flow and deformation of the RBC. Numerical procedures were developed for computing the deformation of a capsule as a model of RBC in simple shear flow by using a boundary-element method (Ramanjan and Pozrikidis, 1998), and by considering the membrane bending stiffness (Pozrikidis, 2001). Bluestein et al. (2008) conducted a numerical study of the role of microcalcifications in plaque vulnerability in an eccentric stenosis model, using a transient fluid–structure interaction analysis through a two-dimensional simulation. The deformation of RBCs was simulated by Tanaka and Koshizuka (2007) and Tsubota et al. (2006) by using a particle method. Neutrophils passing through a constriction in a cylindrical capillary vessel were simulated by Shirai et al. (2002). Luo and Pedley (1998) investigated the effect of wall inertia on self-excited oscillations in collapsible channel flow by solving the full coupled two-dimensional membrane-flow equations. They found that the critical value of tension below which oscillations arise at fixed Reynolds number increased with increasing wall inertia. Zhu and Chin (2008) simulated flexible elastic filaments interacting with a viscous pulsatile flow in two dimensions using the immersed boundary method. Barthès-Biesel et al. (2002) compared three membrane constitutive-laws governing the deformation of a two-dimensional capsule suspended in hyperbolic pure straining flow. The cells were modeled as deformable capsules, composed of an elastic membrane. They suggested that the existence of a possible hydrodynamic mechanism could be used to interpret the observed maximum leukocyte aggregation in shear flow. Jadhav et al. (2007) investigated the collision process between two modeled cells, interacting in linear shear flow through two-dimensional numerical simulation. The interaction between the deformation and flow around the object were considered. Karagiozis et al. (2005) numerically investigated nonlinear vibrations for empty and fluid-filled circular cylindrical shells. They studied fluid–structure interaction based on linear potential flow theory, that is, they did not take fluid viscosity into account.

In the analysis of the deformation of compliant or elastic cylinders, Étienne and Pelletier (2005) developed a general formula for computing the interactions between incompressible flow and hyperelastic solids and their sensitivities. They obtained the deformed shape of an empty elastic cylinder in a uniform flow. The effects of wall compliance on flow have been studied for the laminar–turbulent transition (Cros et al., 2003), control of unsteady separation on a cylinder with a compliant wall (Pal and Sinha, 1998), and drag reduction (Endo and Himeno, 2001) from an engineering point of view. Gad-el-Hak (2002) reviewed compliant coatings for drag reduction, and described the drag reduction due to the

laminar-to-turbulent transition delay as it relates to the compliance of dolphin epidermis. Wang et al. (2005) showed that compliant surfaces retarded the development of secondary instabilities during the early stages of laminar–turbulent transition, and edge-generated waves increased the amplitudes of the original 2-D and 3-D TS waves during the later stages of fundamental wave breakdown. Darekar and Sherwin (2001) considered flow past square-section cylinders with spanwise geometric deformation in order to investigate its influence on wake structures and drag reduction. They found that the drag was substantially lower than that of a straight cylinder.

The effects of internal flow of the compliant objects on its deformation have not been considered in previous studies. Therefore, we needed to develop a numerical procedure to simulate induced flows inside the compliant objects deformed by stresses due to external flow. In this study, we consider the interactions between the internal flow, external flow and deformation through internal and external forces acting on the membrane. The internal and external flows were obtained by solving the Navier–Stokes equations, and the deformation of the membrane, consisting of a network of mass-spring-damper (MSD) units, was calculated by solving the equation of motion for a MSD system by using the fourth-order Runge-Kutta method. After validating the simulation method described in Section 4, we tested the effects of the mechanical properties of the membrane on deformation by changing the stiffness and damping coefficients of the MSD unit. The deformed shapes are presented in Section 5.1. The cross-section of the deformed cylinder was found to oval, with its major axis perpendicular to the main flow direction. The flow characteristics represented by the drag coefficient and Strouhal number of the shed vortices from the deformed cylinder are compared to those of a rigid circular cylinder. The effects of stiffness and damping of the membrane of the compliant object on deformation and flow fields around and inside the deformed cylinder are discussed in this section. The drag coefficient of the oval cylinder is larger than that of the circular cylinder, and increased with decreasing stiffness. The internal and external flows of the deformed cylinder are shown in Section 5.2. The partial vibration at the rear, caused by shedding vortices, induces oscillating internal flows between two antinodes of the vibrating membrane. Thus, velocity fluctuations of the external flow influence the internal flow in the compliant object through deformation of the membrane, if the object has high ductility.

2. Model of the compliant cylinder

The calculation domain and compliant cylinder, whose cross-section is initially a circle with radius R, are shown in Fig. 1. The width, w, of the side boundaries of the calculation domain is $8R$. Before setting the width, we checked the C_d of a rigid circular cylinder, and the deformed shape of a compliant cylinder, for various w. These values did not change when w was larger than or equal to $8R$. The slip condition is given at the side-boundaries. This means that the cylinder is in uniform flow. The out-flow boundary is located at a distance of $8R$ downstream from the center of the cylinder. The in-flow boundary is located at a distance of $2R$ upstream from the center of the cylinder. Uniform flow with free stream velocity, U, is applied at the boundary. The compliant cylinder is a model of a cell whose center is fixed at the origin of the coordinate system, but is allowed to deform. The reference mechanical properties of the membrane are those of latex gum ($k = 1.0$, $c = 0.05$). We consider the membrane softer in this study in the condition where k is lower than this value. The no-slip condition is applied to the surface of the cylinder.

The membrane of the cylinder is modeled by a network of units of a mass-spring-damper system, as shown in Fig. 2. The unit is a Voigt model (masses are connected by both a spring and damper). Sugiyama and Hirai (2006) simulated a crawling soft robot with a two-dimensional circular MSD network, and Endo and Himeno (2001) represented the compliant surface of a cylinder by using the Voigt model. According to these studies, it is reasonable to represent the mechanical characteristics of the compliant matter by means of a network system of MSD units. Therefore, the MSD unit given by the Voigt model is applied to the components of the membrane and imaginary core structure of the compliant object, and the connections of the membrane and core structure, as shown in Fig. 2. Initially, the point masses, $m_{\mathrm{out},i}$ are distributed on a circle of radius R, which is the membrane. The points of the mass, $m_{\mathrm{in},i}$, on a circle of radius R' (R':$R = 0.8$:1.0) are the imaginary core structures. The core structure represents a base of fiber structures, such as microfilaments supporting the membrane. The MSD units connecting $m_{\mathrm{out},i}$ and $m_{\mathrm{in},i}$ are the model of fiber structures between the membrane and the core structure.

The forces acting on the membrane are evaluated at the position of each mass, as shown in Fig. 3. The compressive or expansive forces are calculated from the pressures on both sides of the membrane, and the friction force on the membrane is calculated from the shear stress by solving the equation of external fluid motion of the cylinder. To convert the stresses to forces, the stresses are multiplied by the local area, A_i, represented by half the distance between adjacent masses times the unit length in the direction perpendicular to the figure. The minimum number of joints of MSD units

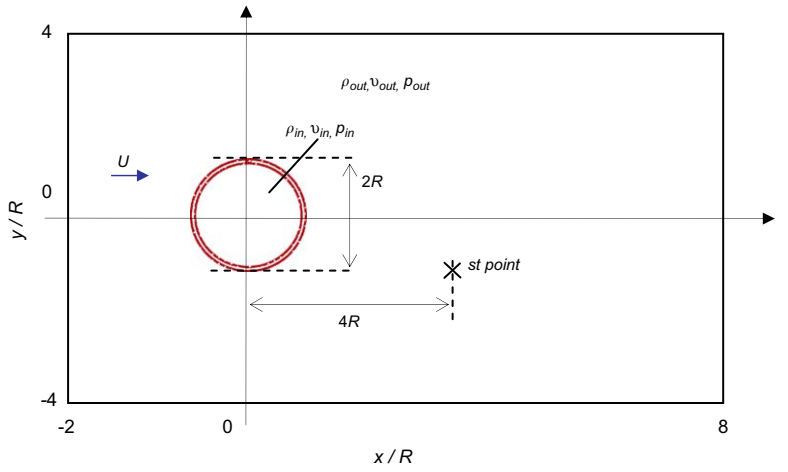

Fig. 1. Calculation domain around a compliant cylinder. The point denoted as 'st point' is a position at which velocity fluctuations due to shedding vortices are measured.

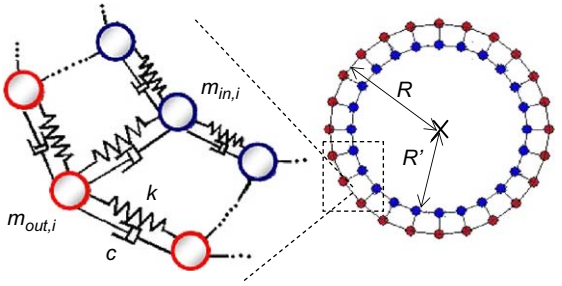

Fig. 2. Model of a compliant cylinder. MSD unit is represented by the Voigt model. R': $R = 0.8{:}1.0$, $i = 0,\ldots,N_m-1$, $N_m = 48$, k: spring constant and c: damping coefficient.

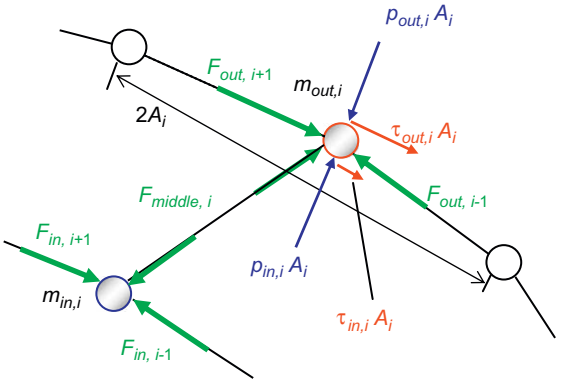

Fig. 3. Forces acting on an objective mass. Here, A_i represents the area based on the straight distance between m_{i-1} and m_{i+1}, $p_{\mathrm{out},i}$ and $p_{\mathrm{in},i}$ are the pressures due to external and internal flows, respectively, and $\tau_{\mathrm{out},i}$ and $\tau_{\mathrm{in},i}$ are the shear stresses.

necessary to express the smooth deformation of the membrane is 48, which was used in order to minimize the calculation time. The core structure consists of 48 MSD units, and the connections between the membrane and core structure are also 48. The core structure is assumed to be an imaginary structure in this paper and not affected internal flows.

The forces due to the network of MSD units are calculated by simultaneous equations, as follows:

$$m_{\mathrm{out},i}\frac{d^2\vec{x}_{\mathrm{out},i}}{dt^2} = \vec{F}_{\mathrm{out},i-1} + \vec{F}_{\mathrm{out},i+1} + \vec{F}_{\mathrm{middle},i} + \vec{p}_{\mathrm{out},i}A_{\mathrm{out},i} + \vec{\tau}_{\mathrm{out},x}A_{\mathrm{out},i} + \vec{p}_{\mathrm{in},i}A_{\mathrm{in},i} + \vec{\tau}_{\mathrm{in},x}A_{\mathrm{in},i},$$
$$m_{\mathrm{in},i}\frac{d^2\vec{x}_{\mathrm{in},i}}{dt^2} = \vec{F}_{\mathrm{in},i-1} + \vec{F}_{\mathrm{in},i+1} + \vec{F}_{\mathrm{middle},i},$$
$$\vec{F} = -k\vec{x} - c\dot{\vec{x}},\ A_i \approx \frac{1}{2}|\vec{x}_{i+1} - \vec{x}_{i-1}|. \tag{1}$$

Here, the suffixes 'out', 'in' and 'middle' of the resistance force, F, refer to the membrane, representative core structure and connection between the membrane and core structure of the cylinder, respectively. The suffixes '$i+1$' and '$i-1$' on F indicate the forces determined by the adjacent MSD unit attached to the ith mass. The notations $p_{\mathrm{out},i}$ and $p_{\mathrm{in},i}$ are the pressures calculated in the external and internal flows, respectively. The $\tau_{\mathrm{out},i}$ and $\tau_{\mathrm{in},i}$ are the shear stresses calculated in the external and internal flows, respectively. The boundary conditions for solving the internal flow are given by displacement velocities at objective mass positions of the membrane as a result of deformation.

3. Governing equations of fluid motion

The external and internal flows of the compliant cylinder were obtained by solving the incompressible Navier–Stokes equations in the calculation area, as shown in Fig. 1. The nondimensional governing equations, expressed in terms of vorticity and stream function, are written as

$$\frac{\partial\omega}{\partial t} + u\frac{\partial\omega}{\partial x} + v\frac{\partial\omega}{\partial y} = \frac{1}{\mathrm{Re}}\left(\frac{\partial^2\omega}{\partial x^2} + \frac{\partial^2\omega}{\partial y^2}\right). \tag{2}$$

Poisson's equation relating the stream function and vorticity is shown as follows:

$$\frac{\partial^2\varphi}{\partial x^2} + \frac{\partial^2\varphi}{\partial y^2} = -\omega, \tag{3}$$

where φ denotes the stream function, ω represents the vorticity and u and v are the components of velocity in the x and y directions, respectively. The finite element scheme based on the Galerkin method is used to obtain the stream function and vorticity at the contact points of the triangular mesh and velocity at the center of the mesh. The number of mesh points in the calculation domain is 3850 points outside of the cylinder, and 259 points inside of the cylinder. The pressure is obtained by solving Poisson's equation

$$-\frac{1}{2}\nabla^2 p = \frac{\partial^2\varphi}{\partial x^2}\frac{\partial^2\varphi}{\partial y^2} - \left(\frac{\partial^2\varphi}{\partial x\partial y}\right)^2. \tag{4}$$

The procedure used to solve the coupled problem is shown in Fig. 4. After initialization, the stream function and vorticity of both the inside and outside flows are calculated by Eq. (3) at time t^*. The velocities u and v are computed from the stream function. The pressure is calculated by using Eq. (4), and the shear stress is computed by using the velocity gradient on the membrane. To obtain the deformation of the compliant cylinder, the pressure and shear stress on the membrane are substituted into Eq. (1), and the positions of the masses are calculated by using a fourth-order Runge-Kutta method. The stream function and vorticity of the internal flow presented in Eq. (3) are calculated under the boundary condition given by the aforementioned steps. Since the conservation of mass of the internal fluid must be satisfied, the volume of the compliant cylinder after deformation is adjusted by the Level-Set method [see Chang et al. (1996)]. Namely, the size changes in proportion to the ratio of the volume before and after deformation. The triangular mesh in the calculation domain is generated again to fit the body shape of the column after deformation. The time is advanced from t^* to $t^* + dt^*$ (dt^* being the time step), and the calculation is repeated as necessary.

4. Verification of the simulation

The simulation was verified by checking the values of the drag coefficient and Strouhal number of the rigid circular cylinder, rectangular cylinder and elliptic cylinder. Fig. 5 shows the drag coefficient and Strouhal number of the rigid circular cylinder for $\mathrm{Re} \leq 5 \times 10^3$ obtained in this simulation, as well as the experimental data. The drag coefficient for several Reynolds numbers is in good agreement with the experimental data, which is depicted by the broken line (red) in

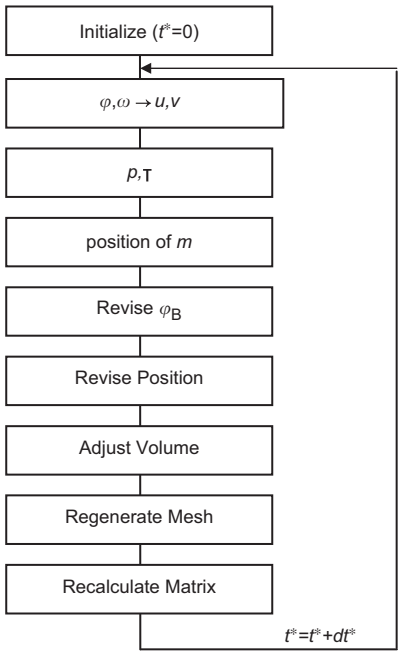

Fig. 4. Flow chart of the simulation.

Fig. 5, and reported in textbooks [e.g. Munson et al. (2002)] and handbooks [e.g. The Japan Society Mechanical Engineering (2006)]. The Strouhal number related to the vortex shedding is 0.25. This value is slightly larger than the experimental data, depicted by the dotted line (blue), which is a common feature of two-dimensional simulations. Vortex shedding was not observed at $\mathrm{Re} \leq 100$. We concluded that the flow around the circular cylinder in our Reynolds number range is reasonably well captured by this simulation.

In order to confirm the drag coefficient for a noncircular cross-section of the cylinder in this simulation, we obtained C_d for rigid rectangular and elliptical cylinders. The drag is calculated by integration of surface pressures and shear stresses on the surface of the cylinders. The ratio of the vertical to horizontal length was 2.0 for both cylinders. The value of C_d for the elliptical cylinder was 1.6 in the Reynolds number range shown in Fig. 6, and that of the rectangular cylinder was 2.0. These values seem reasonable compared to the experimental data. This shows that the flows around the noncircular cylinders at Reynolds numbers below 10^3 are correctly simulated.

We confirmed the deformation of the compliant cylinder by comparing our results with the results of Endo and Himeno (2001), obtained by direct numerical simulation (DNS) for a similar cylinder in uniform flow. Although the internal flow of the body was not taken into account in their calculation by DNS, both shapes were quite similar. Therefore, we believe that our simulation yields reasonable results for deformation.

5. Results and discussion

5.1. Effect of stiffness, damping coefficient and Reynolds number on deformation

We carried out simulations for a compliant cylinder filled with water and immersed in water for various values of k, c and Re. We investigated the influence of these parameters on the deformation and flow fields around the compliant cylinder. The internal flow was also calculated for effects of internal fluid viscosity on the deformation and vibration of the compliant cylinder. The deformed shape obtained by this calculation is compared with that obtained by the calculation without considering the internal flow, as shown in Fig. 7. These shapes were obtained at the nondimensional time $t^* = \frac{3}{4} T_{N0}$, where T_{N0} is the time at which the aspect ratio (AR) is at a maximum during the natural oscillation, after the beginning of the calculation. In order to see the shape more clearly, the distortion from the original shape is magnified 10 times. The difference in AR between these cases is approximately 1% larger than the spatial resolution.

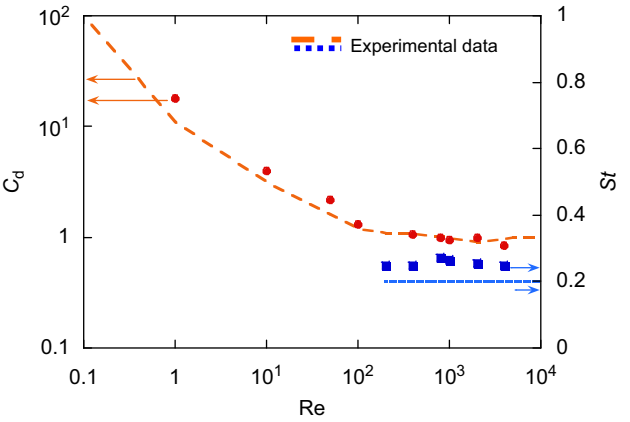

Fig. 5. Drag coefficient C_d and Strouhal number St of the rigid circular cylinder. The red broken line is C_d experimental data, and the blue broken line is St from reference JSME (2006). (For interpretation of the references to color in this figure legend, the reader is referred to the web version of this article.)

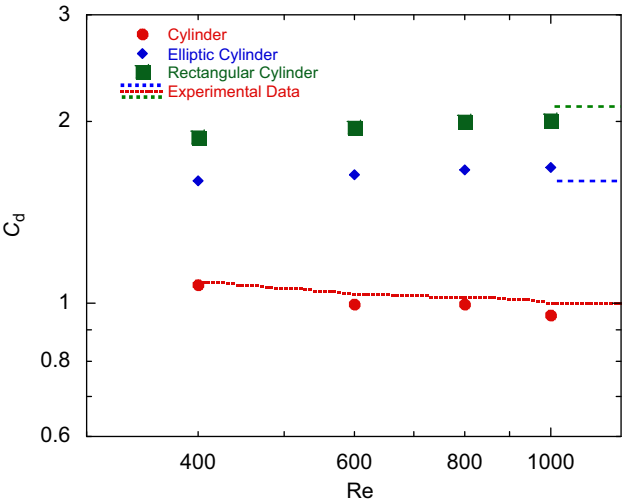

Fig. 6. Drag coefficient C_d of rigid elliptical and rectangular cylinders with aspect ratios of 2.0. Experimental data at Reynolds number $Re > 10^3$ are given in reference JSME (2006).

This difference is important with respect to the effect of the internal flow on deformation. As shown in Fig. 7, the direction of the internal flow coincides with that of the movement of the membrane when considering internal flow.

Fig. 8 shows evolution of the AR of the cross-section and velocity fluctuation due to the shedding vortices at the 'st point', as shown in Fig. 1. The shapes at the corresponding times are represented at the top of the figure and are magnified by 10 times. The compliant cylinder first oscillates with natural frequency $(1/T_N)$. Since the main stream velocity increases suddenly from 0 to U at the start of the calculation, a step-like force acts on the compliant cylinder. Therefore, the cylinder initially vibrates with period T_N in natural oscillation with mode 2. We confirmed, by changing the spring constant k (from 0.1 to 2.0), that the natural frequency $(1/T_N)$ increases proportionately to the square-root of k. The vortices are shed regularly with frequency $(1/T_K)$ in this case. The shedding frequency of vortices is six times higher than that of the natural frequency $(1/T_N)$ of the cylinder. As the stiffness increases, the cylinder becomes harder, and T_N decreases. Thus, the cylinder constructed of a material with $1/T_N \geq 1/T_K$ is no longer soft. Since the damping was set in this model, the amplitude of the AR-oscillation gradually becomes smaller. We confirmed that T_N decreases in proportion to the square-root of k, and T_K decreased in proportion to k. Thus, in this condition, because the difference by T_K was much smaller than the difference by k, T_N/T_K decreased in proportion to the square-root of k. On the other hand, length in y-axis, L_y, decreased with increasing k. Thus, as T_N decreased in proportion to the root of k,

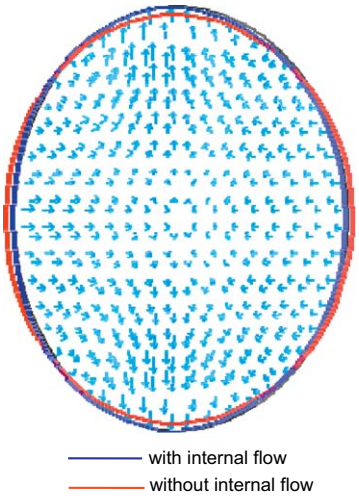

Fig. 7. Comparison of shapes in the case of a compliant cylinder with and without internal flow at $t^* = \frac{3}{4}T_{N0}$ for Re = 400, $k = 1.0$ and $c = 0.05$. Here, T_{N0} is the time at which L_y is at a maximum. The arrows show the velocity vectors of internal flows. The shapes are shown at 10 times magnification.

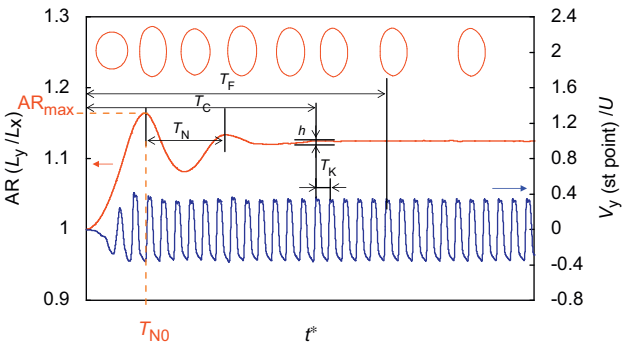

Fig. 8. Evolutions of the shape of the deformed compliant cylinder. Figures are magnified 10 times. The aspect ratio, AR, of the cross-section (red line) and velocity fluctuation, v_y, due to the shedding vortices (blue line). Here, $k = 1.0$, $c = 0.05$ and Re = 400. (For interpretation of the references to color in this figure legend, the reader is referred to the web version of this article.)

the nondimensional number (natural frequency and inverted shear rate) $T_N\, U/L_y$ decreased in proportion to the square-root of k.

When the amplitude becomes smaller than $h = 0.001L_y$, the shape of the cross-section is regarded as having converged at $t^* = T_C$. We allowed for sufficient calculation time to evaluate the final shape, so that the final shape of the cross-section was defined as the shape at $t^* = T_F = T_C + 5T_K$. The final shape of the cross-section is oval with a convex surface at the rear. Fig. 9 shows the influence of Re in a range from 200 to 800 on the AR of the final shape. The AR increased with increasing Re for the case of $k = 1.0$ and $c = 0.05$. The effect of parameters, k and c, on the final shape is discussed later.

After $t^* = T_F$, the vibration with the shedding frequency of vortices, f_K ($= 1/T_K$), becomes dominant, as shown in Fig. 8. Fig. 10 shows the change in AR and velocity fluctuation, v_y, at the 'st point' during T_K. The period of AR coincides with that of velocity fluctuation due to shedding vortices. The average deviation from the circle is approximately 0.1%. The evolution in shape is shown, magnified 200 times in order to more easily visualize the deformation. It was observed that the membrane near the positions where vortices form oscillates at the period of the shedding vortices. Fig. 12 shows the local amplitude of the membrane-oscillation to the angle measured from the front stagnation point. Here, θ is the angle measured from the upstream stagnant point of the compliant cylinder. The amplitude is at a maximum at 70° and 160°, which are out of phase, as seen in Fig. 11 and 12.

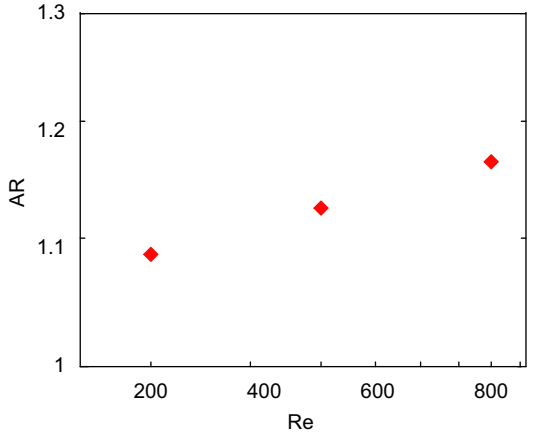

Fig. 9. Aspect ratio, AR, of the final shape versus Reynolds number Re ($k = 1.0$ and $c = 0.05$).

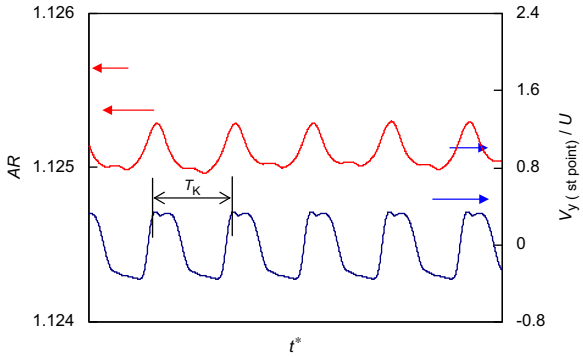

Fig. 10. Change in AR (red line) and velocity fluctuation (blue line) measured at the 'st point' after T_F for $k = 1.0$, $c = 0.05$ and $\mathrm{Re} = 400$. (For interpretation of the references to color in this figure legend, the reader is referred to the web version of this article.)

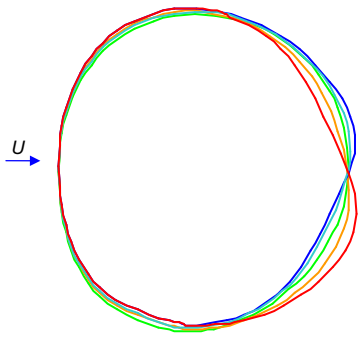

Fig. 11. Change in the cross-sectional shape of the compliant cylinder vibrated by shedding vortices. Here, colored lines show the figures at different times: red, T_K; orange, $\frac{1}{8}T_K$; light green, $\frac{2}{8}T_K$; green, $\frac{3}{8}T_K$; blue, $\frac{4}{8}T_K$ for $k = 1.0$, $c = 0.05$ and $\mathrm{Re} = 400$. The figures are magnified 200 times. For interpretation of the references to color in this figure legend, the reader is referred to the web version of this article.

Changes in shape of the compliant cylinder for different combinations of k and c are shown in Fig. 13. Under these conditions, the final shape for each condition is similar to an oval cylinder with the major axis perpendicular to the main direction of flow. This shape is similar to the result of the low-density liquid drop rising in a high-density liquid, observed by Myint et al. (2006), even though the drop is an axisymmetric body.

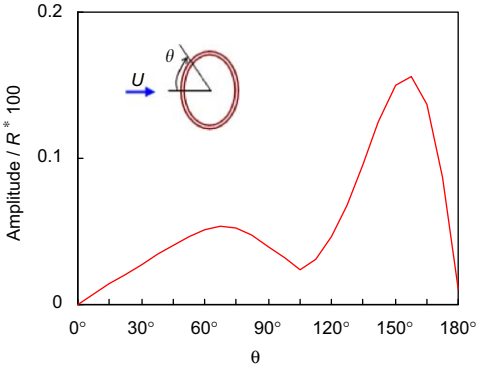

Fig. 12. Amplitude of the membrane vibration by shedding vortices for $k = 1.0$, $c = 0.05$ and $\mathrm{Re} = 400$. The maximum amplitude appears at $\theta = 68^\circ$ and 158°. Here, θ is the angle measured from the upstream stagnant point of the compliant cylinder.

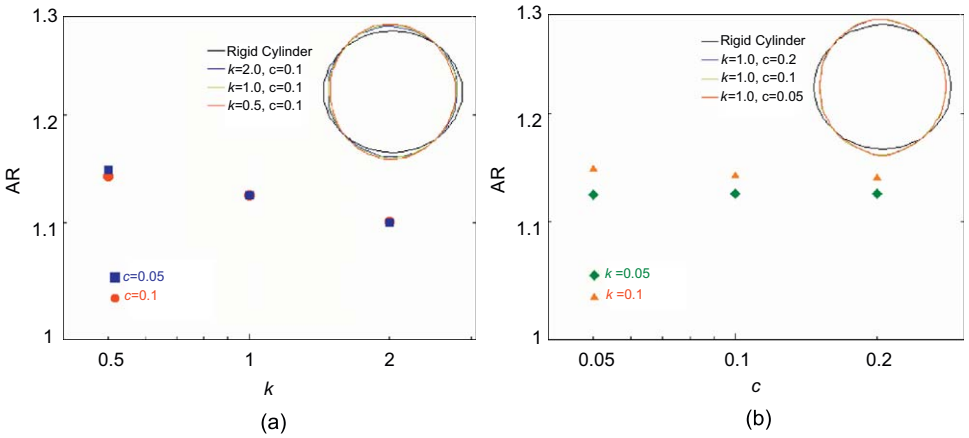

Fig. 13. AR versus k and c at $\mathrm{Re} = 400$; in (a) c is fixed and in (b) k is fixed.

Since it is difficult to describe the difference in shape, the aspect ratio, AR, of the final shape of the compliant cylinder is plotted in Fig. 13 with respect to k and c. As shown in Fig. 13(a), the AR becomes smaller with increasing k, approaching $\mathrm{AR} = 1$, which is the value for the rigid cylinder. In other words, the AR of the compliant cylinder with smaller k becomes larger. On the other hand, the effect of c on the AR is negligible, as seen in Fig. 13(b).

To evaluate the effect of shape on flow characteristics, the drag coefficient, C_d, and the Strouhal number, St, are shown in Fig. 14 for different combinations of k and c. Average values were taken after T_F. The drag coefficient becomes larger than that of the rigid circular cylinder when the cylinder is softer. The same tendency is shown in the results produced by Endo and Himeno (2001). The value of St, however, is not different from that of the rigid circular cylinder. As mentioned before, the shape of the compliant cylinder becomes oval when k is small. Thus, the value of C_d of the deformed compliant cylinder has a value similar to that of the elliptic cylinder, which is larger than that of the circular cylinder and smaller than that of the rectangular cylinder with an AR of 2.0, as shown in Fig. 6. The value of C_d becomes larger with decreasing k at fixed $c = 0.1$, as shown in Fig. 14(a), and with decreasing c at fixed $k = 10.0$, as shown in Fig. 14(b).

The surface pressure distribution in the case of $k = 1.0$ and $c = 0.05$ is presented in Fig. 15. The angle, θ, is measured from the upstream stagnation point in the clockwise direction. The area of positive pressure at the front extends and the negative back pressure becomes larger than that of the rigid circular cylinder. If the cylinder is stiff, in particular if k is large, for example $k = 10.0$, then the deformation is very small. In other words, the deformation is similar to that of the circular cylinder. Thus, the pressure distribution of the compliant cylinder with higher k is similar to that of the rigid circular cylinder.

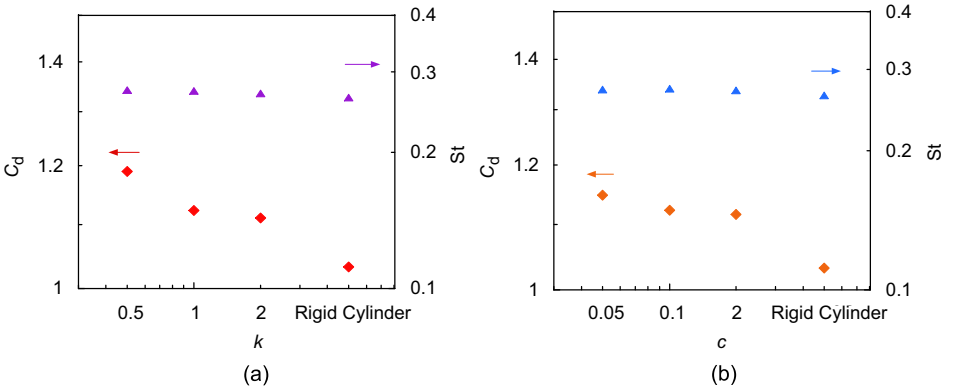

Fig. 14. Drag coefficient C_d and Strouhal number St versus (a) k with $c = 0.1$ and (b) c with $k = 1.0$ (Re = 400).

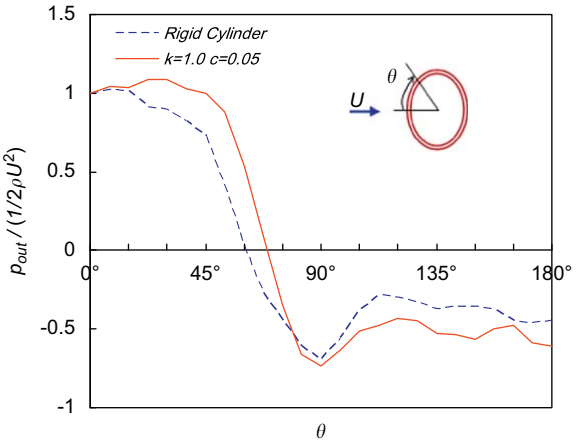

Fig. 15. Pressure distribution on the surface of the deformed cylinder compared with a rigid cylinder for $k = 1.0$, $c = 0.05$ and Re = 400.

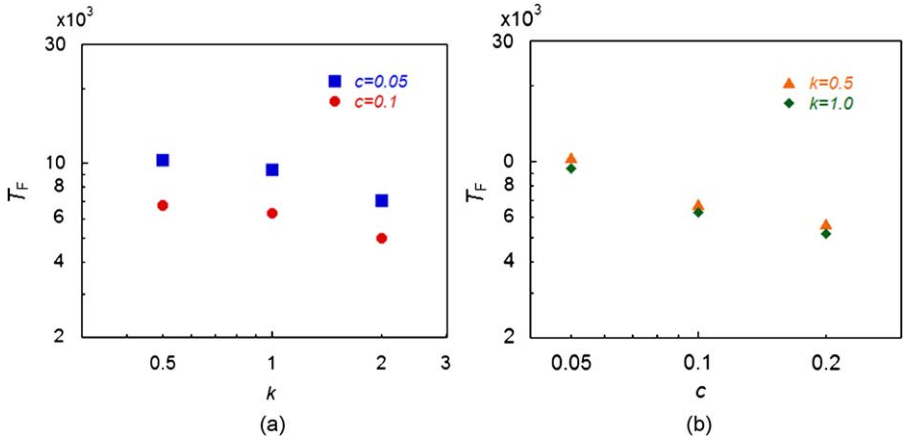

Fig. 16. Required time T_F to achieve the final shape for (a) k and (b) c at Re = 400.

Fig. 16 shows the required time at which the compliant cylinder settled into its final shape. The required time increases with decreasing k, as shown in Fig. 16(a); and decreases with decreases in c, as shown in Fig. 16(b). This means that the compliant cylinder with softer characteristics reaches the final shape more slowly. The effect of the damping coefficient on the required time is larger than that of the stiffness.

5.2. Flow around the deformed cylinder and induced flow in the deformed cylinder

In this section, we discuss the effects of the deformation of the compliant cylinder on internal flow fields.

Fig. 17 shows the internal flow pattern at $\frac{1}{4}\,T_N$ and $\frac{3}{4}\,T_N$ during natural oscillation. The arrow shows the velocity vector, and the color indicates the magnitude of local pressure. The oscillation of mode 2 occurs during T_C, as shown in Fig. 8. The pressure near the center is always high during the oscillation, as seen in the pressure distribution. The flow patterns in the x direction from the center toward the front and rear membrane, and in the y direction from the side membrane toward the center are observed at $\frac{1}{4}\,T_N$. These flows arise from the corresponding membrane-motion due to the oscillation of mode 2. The flow patterns show flow at a saddle point located at the center of the cylinder. The direction of the flow at the saddle point turns 90° every half period of T_N, as seen in Fig. 17. These flow patterns are also observed in the oscillating droplet observed by Trinh and Wang (1982). Therefore, the internal flow pattern is a saddle point flow if an object oscillates with mode 2.

Fig. 18 shows flow fields around and inside the cylinder at $\mathrm{Re} = 400$. The arrow shows the velocity vector and color shows the magnitude of local pressure, the scale of which is shown in the figure. The results of the deformed cylinder are shown in Fig. 18(a) and (b), and that of a rigid circular cylinder at the same Reynolds number is shown in Fig. 18(c). The deformed shapes seen in Fig. 18(a) and (b) are chosen as typical of the deformed compliant cylinder after T_F. The natural oscillation is already damped in the timing. The upstream face of the compliant cylinder became flatter, and the sides were stretched. Consequently, the compliant cylinder has a convex surface on the downstream side. The flow pattern behind the deformed cylinder shows shed vortices aligning regularly, which is similar to the Kármán vortex street seen in the wake of a rigid circular cylinder. Compared with the flow pattern of a rigid circular cylinder, as shown in Fig. 18(c), the average distance between the rear surface of the compliant cylinder and center of a nascent vortex is shorter than that in the case of the rigid circular cylinder. The scale of shed vortices in the case of the compliant cylinder, estimated by the area in which rotating flow is observed, is obviously larger than that of the rigid circular cylinder. This is the cause of the lower back pressure of the deformed compliant cylinder shown in Fig. 15, and is reflected in the difference of the C_d.

The induced flows inside the deformed cylinder are presented in Fig. 18(a) and (b). These flows arise from the motion of the rear membrane forced by the shed vortices. In order to see the details of the induced internal flow, the arrows indicating the velocity vector are magnified by 1000 times, compared to the values of the external flow field. The induced flow is recognized near the back side of the deformed cylinder, as shown in Fig. 18(a). The membrane position at which the flow rises corresponds to the external stagnant point caused by the half saddle flow induced by the shed vortex,

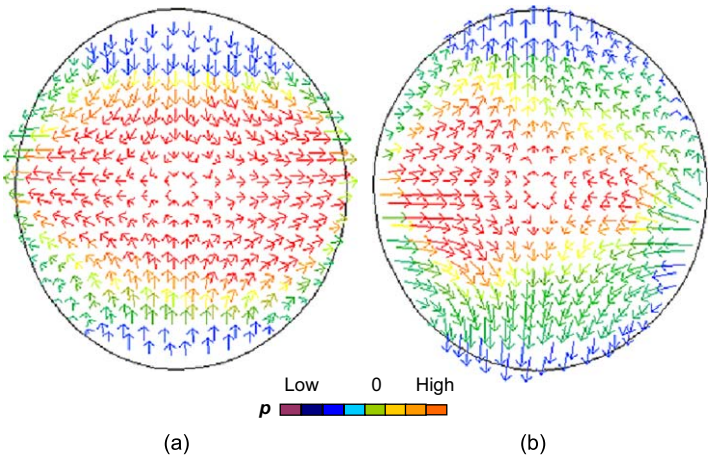

Fig. 17. Internal flow-patterns in the deformed cylinder. These are observed at timing of (a) $\frac{1}{4}T_N$ and (b) $\frac{3}{4}T_N$ for $k = 1.0$, $c = 0.05$ and $\mathrm{Re} = 400$.

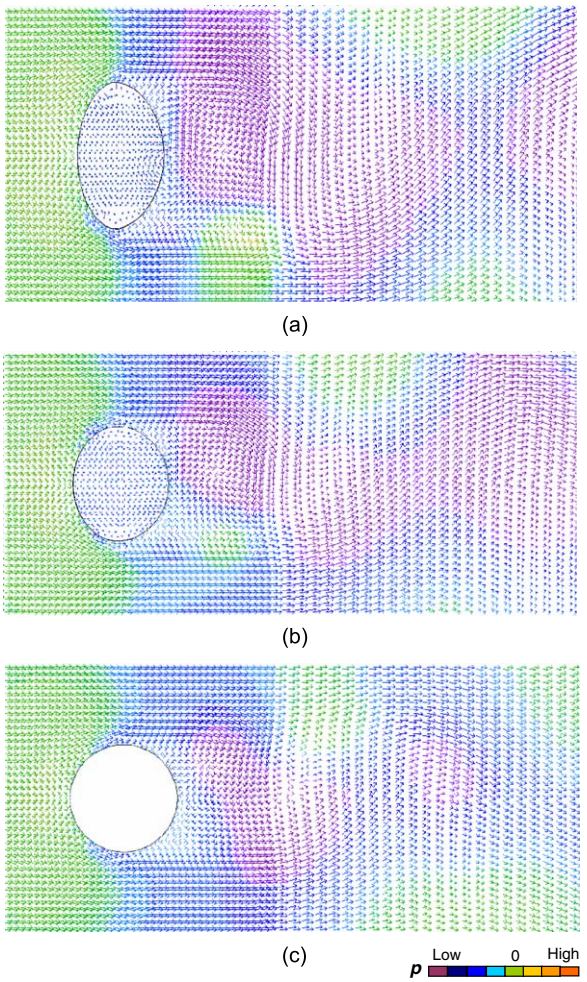

Fig. 18. External and internal flows after T_F for of (a) $k = 0.01$and $c = 0.1$, (b) $k = 1.0$ and $c = 0.1$ and (c) a rigid circular cylinder. The Reynolds number of all flows is $\mathrm{Re} = 400$ (the ranges at which all figures are shown are $-2 < y/R < 2$ and $-2 < x/R < 8$).

whereas the position at which the flow enters corresponds to the low-pressure area near the formed vortex, which appears similar to source and sink flow. The magnitude of the flow depends on the stiffness, as compared with both figures in Fig. 18(a) and (b). Of course, there is no induced flow in the case of the rigid cylinder, Fig. 18(c). Therefore, the flow induced by the oscillation, due to the shed vortices of the compliant cylinder with small k, becomes stronger.

Fig. 19 shows the close-up flow patterns of the deformed cylinder with $k = 1.0$ and $c = 0.1$, shown in Fig. 18(b). The direction of the induced internal flow near the back side changes alternately with the same period of vortex shedding. As shown in Figs. 11 and 12, the rear membrane moves with the change in pressure due to vortex shedding, so that the internal flow is induced by the local deformation due to vortex shedding. In Fig. 20, the distribution of the rms value of velocity fluctuation along the x-axis inside the compliant cylinder is shown. The maxima appear at $x/R = -0.76$, 0.00 and 0.79. The maximum value is 2.8×10^{-3} at $x/R = 0.79$, and the value at the center is approximately 0. The Reynolds number of the internal flow, based on the value at the center, is 1000 times smaller than that of the external flow. Therefore, the internal flow easily follows the motion of the membrane because of the reduced inertia. The relation between the velocity fluctuations at $x/R = -0.76$ and 0.79 is shown in Fig. 21. The phase difference between these points is approximately 180°. Therefore, the directions of these flows are opposite but have the same period. The membrane of the body appears to transform the external flow pattern into the internal flow pattern. In this case, the regular vortex flow in the external region is changed to alternating sink-source flow with the same frequency as the shedding vortices in the internal region of the compliant cylinder.

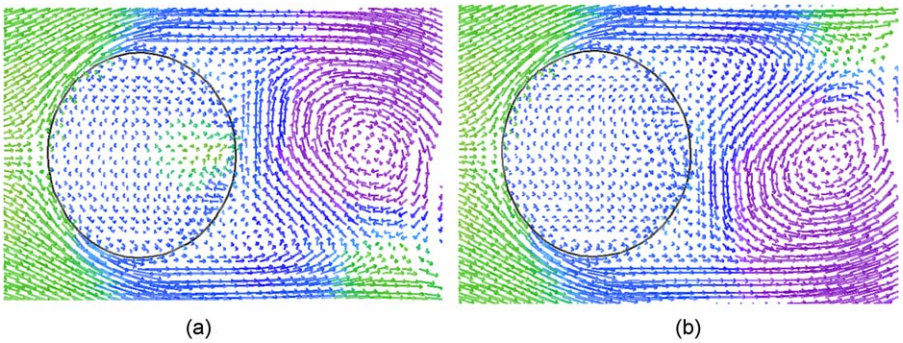

Fig. 19. Internal and external flow patterns of the deformed cylinder measured at (a) T_K and (b) $\frac{1}{2}T_K$ ($k = 1.0$, $c = 0.1$ and $\mathrm{Re} = 400$), the velocity vector are magnified 1000 times (the ranges at which all figures are shown are $-1.5 < y/R < 1.5$ and $-1.5 < x/R < 3$).

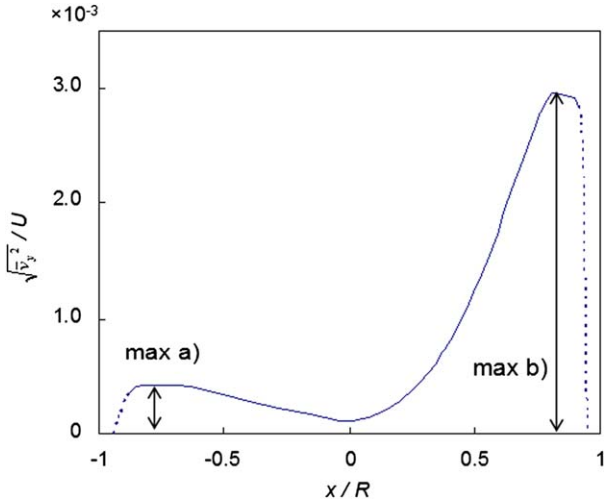

Fig. 20. Distribution of rms values of the velocity fluctuation along the x-axis. The rms value of v_y is represented as $\sqrt{\overline{v_y^2}}$, which is averaged over T_K after T_F. Here, 'max a)' shows the extremum at -0.76 of x/R, and 'max b)' shows the extremum at 0.79 of x/R for $k = 1.0$, $c = 0.1$ and $\mathrm{Re} = 400$.

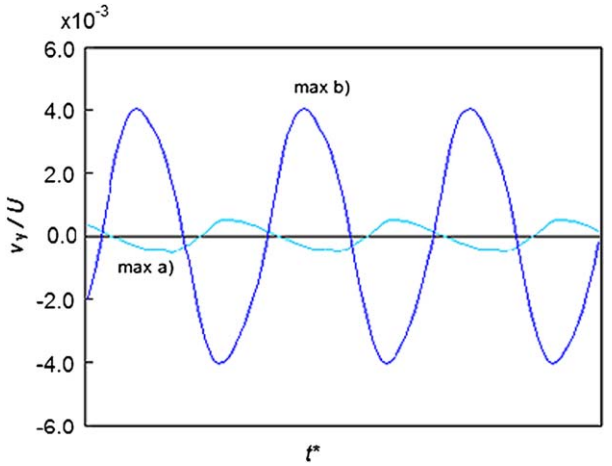

Fig. 21. Velocity fluctuations of v_y observed at positions at which the rms value achieved the extrema 'max a)' and 'max b)' in Fig. 20 for $k = 1.0$, $c = 0.1$ and $\mathrm{Re} = 400$.

6. Conclusion

The deformation of a compliant cylinder filled with fluid in uniform flow, and flow characteristics were investigated by a numerical simulation in order to determine the link between the external and internal flows through a membrane. The compliant cylinder was modeled as a circular cylinder with a surface consisting of a network of mass-spring-damper systems, representing its mechanical characteristics. The compliant cylinder was deformed from that of circular cylinder by the internal and external forces, which were determined by the internal and external flows. The drag coefficient and Strouhal number of shed vortices after deformation were compared with those of a rigid circular cylinder. The shape, initially a circular cylinder, became an oval cylinder, with the major axis perpendicular to the main direction of flow. The ratio of the major to minor axis, i.e., aspect ratio, increased with decreasing stiffness of the membrane. The drag coefficient of the deformed compliant cylinder became larger than that of a rigid circular cylinder, because the back pressure became lower as a result of stronger shed vortices. The rear membrane of the compliant cylinder in uniform flow was found to oscillate with a small amplitude and the same frequency as that of shedding vortices. The membrane oscillation induced internal flows; and the internal flow affected the deformation of the membrane because of the change in internal stress. The internal flow observed near the rear membrane was similar to a combination of sink- and source-flows, the magnitude and direction of which changed with the period of the shedding vortices. The amplitude of the internal flow became larger with smaller stiffness. Since the object with smaller stiffness has high ductility, velocity fluctuations of the external flow influence the internal flow in the compliant object through deformation of the membrane.

References

Barthès-Biesel, D., Diaz, A., Dhenin, E., 2002. Effect of constitutive laws for two-dimensional membranes on flow-induced column deformation. Journal of Fluid Mechanics 460, 211–222.

Bluestein, D., Alemu, Y., Avrahami, I., Gharib, M., Dumont, K., Ricotta, J.J., Einav, S., 2008. Influence of microcalcifications on vulnerable plaque mechanics using FSI modeling. Journal of Biomechanics 41, 1111–1118.

Chang, Y.C., Hou, T.Y., Merriman, B., Osher, S., 1996. A level set formulation of eulerian interface capturing methods for incompressible fluid flows. Journal of Computational Physics 124, 449–464.

Cros, A., Ali, R., Gal, P.LE., Thomas, P.J., Schouveiler, L., Carpenter, P.W., Chauve, M.P., 2003. Effects of wall compliance on the laminar–turbulent transition of torsional Couette flow. Journal of Fluid Mechanics 481, 177–186.

Darekar, R.M., Sherwin, S.J., 2001. Flow past a bluff body with a wavy stagnation face. Journal of Fluids and Structures 15, 587–596.

Endo, T., Himeno, R., 2001. Direct numerical simulation of turbulent flow over a compliant surface. RIKEN Review 40, 7–11.

Étienne, S., Pelletier, D., 2005. A general approach to sensitivity analysis of fluid–structure interactions. Journal of Fluids and Structures 21, 169–186.

Gad-el-Hak, M., 2002. Compliant coatings for drag reduction. Progress in Aerospace Science 38, 77–99.

Jadhav, S., Chanb, K.Y., Konstantopoulos, K., Eggleton, C.D., 2007. Shear modulation of intercellular contact area between two deformable cells colliding under flow. Journal of Biomechanics 40, 2891–2897.

Karagiozis, K.N., Amabili, M., Païdoussis, M.P., Misra, A.K., 2005. Nonlinear vibrations of fluid-filled clamped circular cylindrical shells. Journal of Fluids and Structures 21, 579–595.

Luo, X.Y., Pedley, T.J., 1998. The effects of wall inertia on flow in a two-dimensional collapsible channel. Journal of Fluid Mechanics 363, 253–280.

Munson, B.R., Young, D.F., Okiishi, T.H., 2002. Fundamentals of Fluid Mechanics, 4th Edition. Wiley, Inc., New York.

Myint, W., Hosokawa, S., Tomiyama, A., 2006. Terminal velocity of single drops in stagnant liquids. Journal of Fluid Science and Technology 1, 72–81.

Pal, D., Sinha, S.K., 1998. Controlling unsteady separation on a cylinder with a driven flexible wall. AIAA Journal 36, 1023–1028.

Pozrikidis, C., 2001. Effect of membrane bending stiffness on the deformation of capsules in simple shear flow. Journal of Fluid Mechanics 440, 269–291.

Ramanjan, S., Pozrikidis, C., 1998. Deformation of liquid capsules enclosed by elastic membranes in simple shear flow: large deformations and the effect of fluid viscosities. Journal of Fluid Mechanics 361, 117–143.

Rao, P.R., Zahalak, G.I., Sutera, S.P., 1994. Large deformations of elastic cylindrical capsules in shear flows. Journal of Fluid Mechanics 270, 73–90.

Shirai, A., Fujita, R., Hayase, T., 2002. Transit characteristics of a neutrophil passing through a circular constriction in a cylindrical capillary vessel. Effect of mechanical properties of the cell and constriction geometry. JSME International Journal, Series C 45, 974–980.

Sugiyama, Y., Hirai, S., 2006. Crawling and jumping by a deformable robot. The International Journal of Robotics Research 25, 603–620.

Tanaka, M., Koshizuka, S., 2007. Simulation of red blood cell deformation using a particle method. ''Nagare'' The Japan Society of Fluid Mechanics 26, 49–55.

The Japan Society Mechanical Engineers ed. (JSME), 2006. JSME Mechanical Engineers' Handbook Fundamentals α4: Fluids Engineering. The Japan Society Mechanical Engineers, Tokyo.

Trinh, E., Wang, T.G., 1982. Large-amplitude free and driven drop-shape oscillations: experimental observations. Journal of Fluid Mechanics 22, 315–338.

Tsubota, K., Wada, S., Kamada, H., Kitagawa, Y., Lima, R., Yamaguchi, T., 2006. A particle method for blood flow simulation. Application to flowing red blood cells and platelets. Journal of the Earth Simulator 5, 2–7.

Wang, Z., Yeo, K.S., Khoo, B.C., 2005. Spatial direct numerical simulation of transitional boundary layer over compliant surfaces. Computers & Fluids 34, 1062–1095.

Zhu, L.D., Chin, R.C.Y., 2008. Simulation of elastic filaments interacting with a viscous pulsatile flow. Computer Methods in Applied Mechanics and Engineering 197, 2265–2274.